

## Supporting Information

### **2D NiFe/CeO<sub>2</sub> Basic-Site-Enhanced Catalyst via in-Situ Topotactic Reduction for Selectively Catalyzing the H<sub>2</sub> Generation from N<sub>2</sub>H<sub>4</sub>·H<sub>2</sub>O**

Dandan Wu, Ming Wen<sup>\*</sup>, Chen Gu, and Qingsheng Wu

School of Chemical Science and Engineering, Shanghai Key Laboratory of Chemical Assessment and Sustainability, Tongji University, 1239 Siping Road, Shanghai 200092, R. P. China.

Corresponding Authors

\*Ming Wen: E-mail: [m\\_wen@tongji.edu.cn](mailto:m_wen@tongji.edu.cn).

## **1. EXPERIMENT SECTION**

### **1.1. Chemicals**

All chemicals were commercial and used without further purification. Nickel chloride hexahydrate ( $\text{NiCl}_2 \cdot 6\text{H}_2\text{O}$ , Sinopharm Chemical Reagent Co., Ltd.,  $\geq 98\%$ ), Ferrous sulfate heptahydrate ( $\text{FeSO}_4 \cdot 7\text{H}_2\text{O}$ , Sinopharm Chemical Reagent Co., Ltd.,  $\geq 99.0\%$ ), Cerium nitrate hexahydrate ( $\text{Ce}(\text{NO}_3)_3 \cdot 6\text{H}_2\text{O}$ , Aladdin Chemistry Co., Ltd, 99.5%), Aluminum chloride hexahydrate ( $\text{AlCl}_3 \cdot 6\text{H}_2\text{O}$ , Aladdin Chemistry Co., Ltd, 97.0%), hydrazine monohydrate ( $\text{N}_2\text{H}_4 \cdot \text{H}_2\text{O}$ , Aladdin Chemistry Co., Ltd, 98%), Ethylene glycol ( $\text{C}_2\text{H}_6\text{O}_2$ , Sinopharm Chemical Reagent Co., Ltd.,  $\geq 99.0\%$ ), ethanol absolute ( $\text{C}_2\text{H}_5\text{OH}$ , Sinopharm Chemical Reagent Co., Ltd.,  $\geq 99.7\%$ ), hydrochloric acid (HCl, Sinopharm Chemical Reagent Co., Ltd., 37%), Sodium hydroxide (NaOH, Sinopharm Chemical Reagent Co., Ltd., 96%), Collodion were purchased from Shanghai Ling feng Chemical Reagent Co. Ltd..

### **1.2. Synthesis of 2D NiFeCe-hydroxide complex**

The 2D NiFeCe-hydroxide complex were synthesized through the dynamics controlling coprecipitation process. Taking  $\text{Ni}_6\text{Fe}_4\text{Ce}$ -hydroxide complex for example, 60 mL  $\text{NiCl}_2$  (25 mM), 40 mL  $\text{FeSO}_4$  (25 mM) and 10 mL  $\text{Ce}(\text{NO}_3)_3$  (25 mM) mixed aqueous solution were added into a beaker with the bottom sealed by collodion membrane. And the preparation of collodion membrane is based on our previous report.<sup>1</sup> Then the above-mentioned beaker was vertically immersed into a bigger beaker with 100 mL NaOH (100 mM) to precipitate  $\text{Ni}^{2+}$ ,  $\text{Fe}^{2+}$  and  $\text{Ce}^{3+}$ , after 1h reaction, took the smaller beaker out of the bigger beaker and removed the collodion membrane. Then the 2D  $\text{Ni}_6\text{Fe}_4\text{Ce}$ -hydroxide complex was obtained, and washed thoroughly by deionized water and ethanol for further synthesis of 2D  $\text{Ni}_{0.6}\text{Fe}_{0.4-0.1}\text{CeO}_2$  nanocomposites.

### **1.3. Synthesis of 2D NiFe/CeO<sub>2</sub> nanocomposites**

The 2D NiFe/CeO<sub>2</sub> nanocomposites were synthesized by in-situ topotactic reducing the obtained NiFeCe-hydroxide complex. In a typical procedure, 20 mg obtained NiFeCe-hydroxide complex and 0.2g NaOH were dispersed in 20ml ethylene glycol

(EG) then stirred until solid dissolved, then were transferred to a 30 mL Teflon-lined stainless-steel autoclave, maintained at 160 °C for 12 h. After the reaction was cooled to room temperature, the NiFe/CeO<sub>2</sub> nanocomposites were collected at the bottom of the container. The products were alternately washed by ethanol and deionized water, then dried in a vacuum oven for the following experiment. By changing the initial amount of NiCl<sub>2</sub>, FeSO<sub>4</sub> and Ce(NO<sub>3</sub>)<sub>3</sub> for NiFeCe-hydroxide complex, we can synthesize serial contrast samples of Ni<sub>x</sub>Fe<sub>1-x-y</sub>CeO<sub>2</sub> catalysts with different molar ratio of NiFe and different content of CeO<sub>2</sub>, such as: Ni<sub>0.7</sub>Fe<sub>0.3-0.2</sub>CeO<sub>2</sub> were synthesized by inputting 70 mL NiCl<sub>2</sub> (25 mM), 30 mL FeSO<sub>4</sub> (25 mM) and 20 mL Ce(NO<sub>3</sub>)<sub>3</sub> (25 mM). When without Ce(NO<sub>3</sub>)<sub>3</sub> can obtained NiFe NPs, while without NiCl<sub>2</sub> and FeSO<sub>4</sub> can get CeO<sub>2</sub> nanosheets.

#### **1.4. Synthesis of bulk NiFe/CeO<sub>2</sub> nanocomposites**

The bulk NiFe/CeO<sub>2</sub> nanocomposites were synthesized by reducing the obtained NiFeCe-hydroxide complex at 400 °C for 1 h in pure hydrogen.

#### **1.5. Synthesis of NiFe/Al<sub>2</sub>O<sub>3</sub> nanocomposites**

Following the analogous synthetic process of 2D Ni<sub>0.6</sub>Fe<sub>0.4-0.1</sub>CeO<sub>2</sub> nanocomposites, NiFe/Al<sub>2</sub>O<sub>3</sub> nanocomposites were synthesized by inputting 60 mL NiCl<sub>2</sub> (25 mM), 40 mL FeSO<sub>4</sub> (25 mM) and 18 mL AlCl<sub>3</sub> (25 mM) but 60 mL NiCl<sub>2</sub> (25 mM), 40 mL FeSO<sub>4</sub> (25 mM) and 10 mL Ce(NO<sub>3</sub>)<sub>3</sub> (25 mM).

#### **1.6. Characterization**

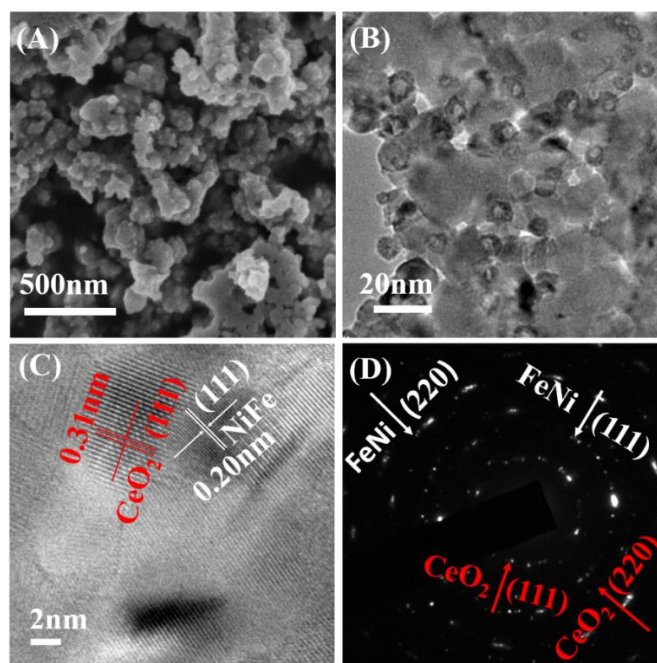
Field-emission scanning electron microscopy (SEM, JEOL, S-4800), transmission electron microscopy and high resolution TEM (TEM, HRTEM, Both of them were obtained by using a JEOL JEM-2100EX microscope) were applied to investigate the size, morphology and microstructural properties of the samples, combined with energy dispersive X-ray spectroscopy (EDS) conducted at 20 keV on a TN5400 EDS instrument (Oxford) for the determination of material composition.. Powder X-ray diffraction (XRD) patterns were obtained using a Bruker D8 (German) diffractometer with a Cu K $\alpha$  radiation source ( $\lambda= 0.1541$  nm) with a scanning angle ( $2\theta$ ) of 25°–85°, operated at 40 kV and 40 mA. Surface elemental valance analysis was performed by

the X-ray photoelectron spectroscopy (XPS) measurements on a RBD-upgraded PHI-5000C ESCA system (Perkin Elmer) using Al K $\alpha$  radiation ( $h\nu=1486.6$  eV). The whole XPS spectrum (0-1100 eV) and the narrower high-resolution spectra were all recorded using a RBD 147 interface (RBD Enterprises, USA). Binding energies were calibrated using the containment carbon ( $C1s=284.6$  eV). CO<sub>2</sub> temperature-programmed desorption (TPD) was carried out on a Micromeritics AutoChem II 2920 automated catalyst characterization system, in which CO<sub>2</sub> was preadsorbed at 323 K for 2 h, then replaced with the carrier gas at 323 K for 2h to purge the physically absorbed CO<sub>2</sub> away from the catalyst surface. After cooled down to room temperature, CO<sub>2</sub> desorption was carried out by raising the temperature at a speed of 10 K min<sup>-1</sup> up to 1073 K, and the released CO<sub>2</sub> was determined by an on-line gas chromatograph equipped with a thermal conductivity detector. The Brunauer–Emmett–Teller (BET) surface areas were measured on Micromeritics ASAP 2020 V 3.00H.

### **1.7. Evaluation of H<sub>2</sub> generation from N<sub>2</sub>H<sub>4</sub>·H<sub>2</sub>O decomposition**

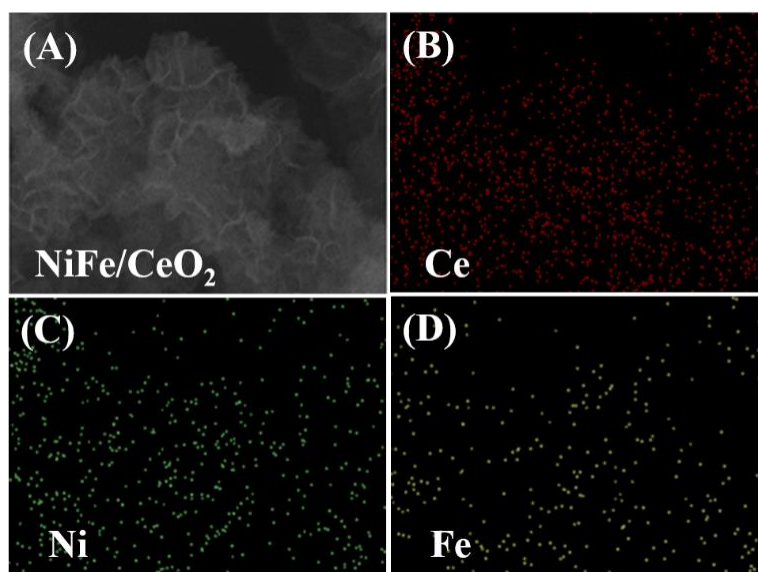
The catalytic decomposition reaction of N<sub>2</sub>H<sub>4</sub>·H<sub>2</sub>O was carried out at 323 K and initiated by injecting N<sub>2</sub>H<sub>4</sub>·H<sub>2</sub>O (0.1 mL) into a two-necked flask containing 50 mg aqueous suspension of above prepared catalyst. The gas released (H<sub>2</sub> and N<sub>2</sub>) during the reaction was passed through HCl solution (1.0 M) before it was measured volumetrically to absorb the by-product of NH<sub>3</sub>, and the volume of the gas released was monitored by the gas burette. In addition, the calculation of H<sub>2</sub> selectivity as well as reaction rate value were based on our previous report.<sup>2</sup>

## 2. Results and Discussion



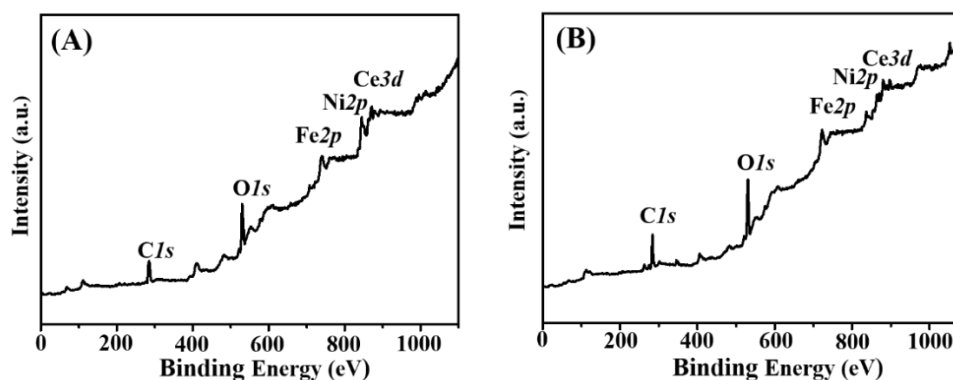
**Figure S1.** SEM (A), TEM (B), HRTEM images (C) and SAED pattern (D) of bulk NiFe/CeO<sub>2</sub> nanocomposites.

The SEM and TEM images of the bulk NiFe/CeO<sub>2</sub> nanocomposites are shown in Figure S1A and S1B, meanwhile, a great agglomeration of NiFe and CeO<sub>2</sub> can be observed. In Figure S1C, HRTEM image of bulk NiFe/CeO<sub>2</sub> nanocomposites presents a crystalline structure with a lattice spacing of 0.20 nm for NiFe (111) planes (white marked) and 0.31 nm for CeO<sub>2</sub> (111) planes (red marked). And the SAED pattern in Figure 1D provides the polycrystalline diffraction rings, indicating a mixed diffraction of NiFe and CeO<sub>2</sub>.



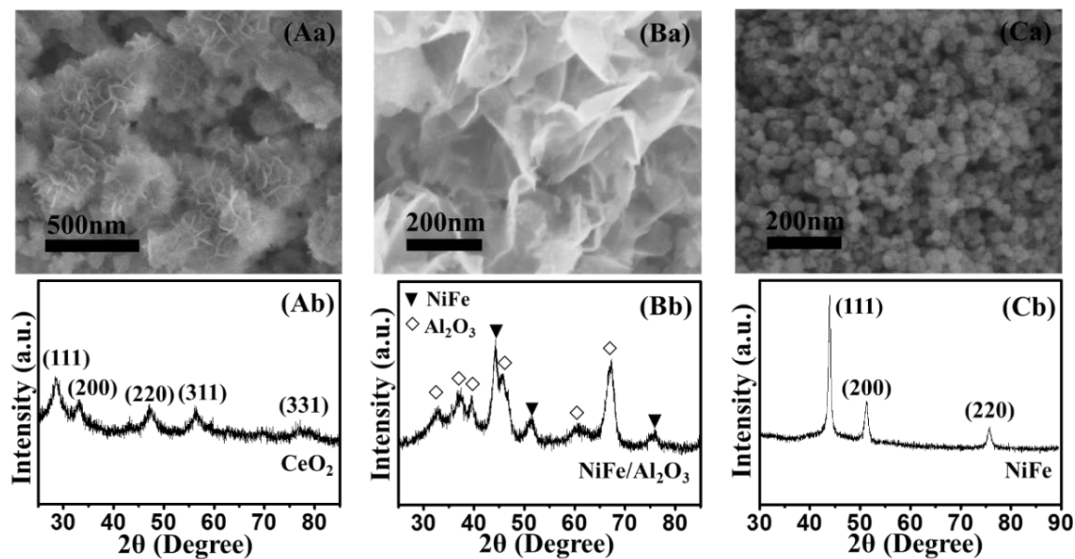
**Figure S2.** (A) SEM image of NiFe/CeO<sub>2</sub>; (B-D) Individual element mappings of Ce, Ni and Fe, respectively.

In Figure S2, elemental mapping was performed to further show the presence of Ce, Ni and Fe in the 2D NiFe/CeO<sub>2</sub> nanocomposites. It can be clearly seen that the element mappings of Fe, Ni and O overlapped with the corresponding SEM image, further indicating the formation of NiFe/CeO<sub>2</sub> nanocomposites.



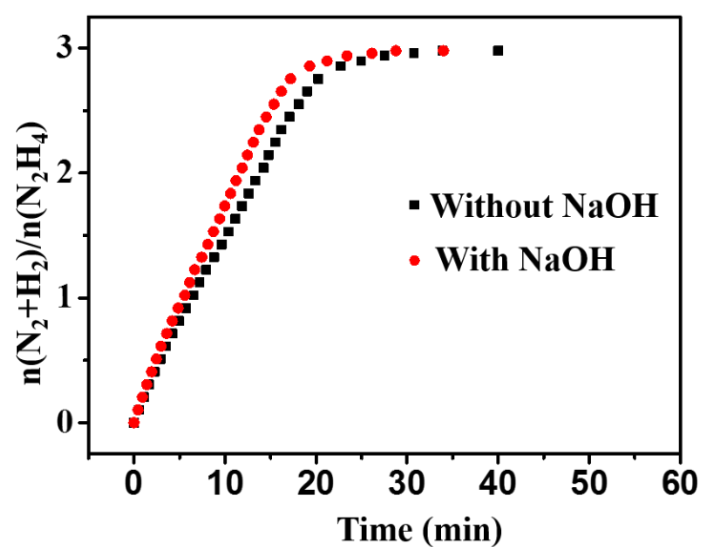
**Figure S3.** XPS analyses of 2D NiFe/CeO<sub>2</sub> nanocomposites (A) and bulk NiFe/CeO<sub>2</sub> nanocomposites (B).

XPS was performed to acquire the valence information of as-designed catalyst and the full spectra of 2D-structured and bulk NiFe/CeO<sub>2</sub> nanocomposites were plotted in Figure S3. In the full spectrum, the numbers of emitted photoelectrons are given as a function of binding energy up to 1100 eV, both 2D and bulk NiFe/CeO<sub>2</sub> nanocomposites present five photoemission peaks (Ce 3d, Ni 2p, Fe 2p, O 1s and C 1s) in the wide spectra.



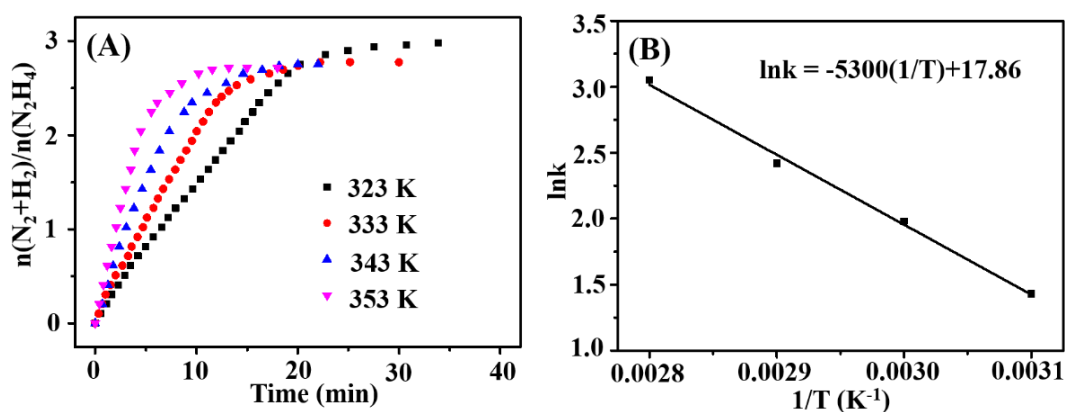
**Figure S4.** SEM images (a) and XRD patterns (b) of CeO<sub>2</sub> nanosheets (A), NiFe/Al<sub>2</sub>O<sub>3</sub> nanocomposites (B) and NiFe NPs (C).

Figure S4 shows the morphology characterization and structure analysis of CeO<sub>2</sub> nanosheets, NiFe/Al<sub>2</sub>O<sub>3</sub> nanocomposites and NiFe NPs. It can be observed that CeO<sub>2</sub> and NiFe/Al<sub>2</sub>O<sub>3</sub> nanocomposites have 2D thin-layer structure, meanwhile, NiFe NPs are uniformly anchored on the surface of Al<sub>2</sub>O<sub>3</sub> nanosheets (Figure S4Ba). When without the protection of support material, NiFe NPs with the diameter of ~50 nm could be obtained (Figure S4Ca). In addition, the XRD patterns of the corresponding catalysts were also investigated in detail. In Figure S4Ab, the XRD pattern of CeO<sub>2</sub> nanosheets shows five broad peaks of (111) at 28.6°, (200) at 33.1°, (220) at 47.5°, (311) at 56.3° and (331) at 76.7°, which agrees well with the lattice of CeO<sub>2</sub> (PDF no. 34-0394). Figure S4Cb reveals three sharp peaks at 44.1°, 51.4° and 75.8° can be indexed to the (111), (200) and (220) planes of the anchored NiFe NPs, which are located between the standard sites of Ni (JCPDF No. 65-0380) and Fe (JCPDF No. 65-4150), confirming the formation of NiFe alloy. The XRD pattern of as-prepared NiFe/Al<sub>2</sub>O<sub>3</sub> nanocomposites is shown in Figure S4Bb and besides the three peaks of NiFe alloy, the other six peaks could be ascribed to Al<sub>2</sub>O<sub>3</sub> (JCPDF No. 47-1308), confirming the fabrication of heterostructured NiFe/Al<sub>2</sub>O<sub>3</sub> nanocomposites.



**Figure S5.**  $n(\text{N}_2+\text{H}_2)/n(\text{N}_2\text{H}_4)$  vs time for 2D NiFe/CeO<sub>2</sub> nanocomposites without NaOH and with NaOH (0.5M) as catalyst promoter.

Figure S5 shows the catalytic performance of 2D NiFe/CeO<sub>2</sub> nanocomposites without NaOH and with NaOH as catalyst promoter for the decomposition of N<sub>2</sub>H<sub>4</sub>·H<sub>2</sub>O. As shown, compared with the catalytic system without NaOH, the catalytic activity improvement of the addition of NaOH is less obvious while the H<sub>2</sub> selectivity remains unchanged. The results strongly support the conclusion that 2D NiFe/CeO<sub>2</sub> nanocomposites could provide solid base as a catalyst promoter to attain high catalytic performance and overcome the drawbacks of aqueous alkali simultaneously.



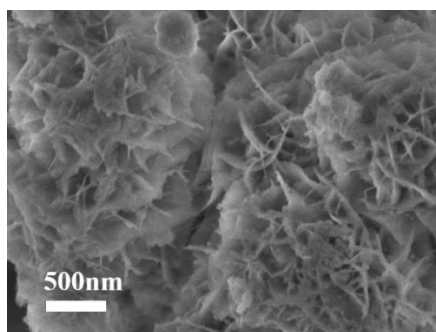
**Figure S6.** (A)  $n(\text{N}_2+\text{H}_2)/n(\text{N}_2\text{H}_4)$  vs time for 2D NiFe/CeO<sub>2</sub> nanocomposites at the temperature range from 323 to 353 K. (B) Arrhenius plots for the decomposition of N<sub>2</sub>H<sub>4</sub>·H<sub>2</sub>O catalyzed by 2D NiFe/CeO<sub>2</sub> nanocomposites at different reaction temperatures.

In order to obtain the activation energy ( $E_a$ ) of the H<sub>2</sub> generation from N<sub>2</sub>H<sub>4</sub>·H<sub>2</sub>O catalyzed by 2D NiFe/CeO<sub>2</sub> nanocomposites, the catalytic reactions were carried out at the temperature range from 323 to 353 K and shown in Figure S6A. As expected, the reaction rate increases with temperature, meanwhile H<sub>2</sub> selectivity decreases a little. Owing to the high reaction temperature can shorten the time of the chemical bond rupture, therefore increase the reaction rate. In addition, the strong Lewis base site derived from the reduced Ce<sup>3+</sup> can weaken the strength of N-H bonds, thus the cleavage of N-N need more energy than N-H. But the energy of the reaction system increases with the reaction temperature, which would increase the possibility of the cleavage of N-N, thus decrease the hydrogen selectivity. Also it clearly shows that the decomposition reaction is zero order. In a zero-order reaction, the Arrhenius equation can be applied to calculate the  $E_a$ . On the basis of the temperature-dependent rate data, the Arrhenius plot of  $\ln k$  vs  $1/T$  was plotted in Figure S6B, calculated from the slope of the linear curve, the activation energy ( $E_a$ ) for the decomposition of N<sub>2</sub>H<sub>4</sub>·H<sub>2</sub>O was estimated to be 44.06 kJ·mol<sup>-1</sup>.

**Table S1.** Catalytic performances of different nanocatalysts for H<sub>2</sub> generation from N<sub>2</sub>H<sub>4</sub> aqueous solution

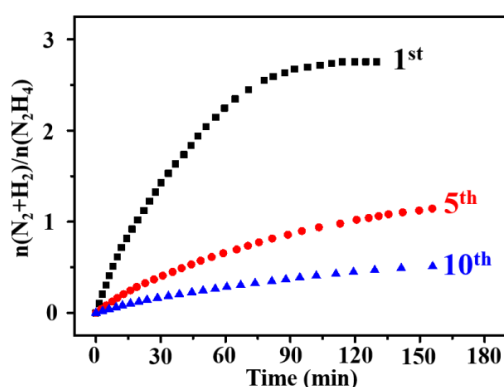
Catalysts	Temperature (°C)	Reaction Time (min)	Selectivity (%)	Additive	Reaction Rate	TOF	Ref.
NiFe	70	90	100	NaOH	-	-	(3)
NiFeMo	50	15	100	NaOH	-	28.8	(4)
NiMoB-La(OH) <sub>2</sub>	50	15	100	NaOH	-	14.3	(5)
Ni <sub>80</sub> Pt <sub>20</sub> @ZIF-8	50	20	100	NaOH	-	90	(6)
RhNi@graphene	25	49	100	NaOH	-	13.7	(7)
Ni <sub>3</sub> Pt <sub>7</sub> /graphene	25	25	100	NaOH	-	68	(8)
NiPt/MA	50	5	100	NaOH	-	160	(9)
Rh/Ni@SiO <sub>2</sub>	25	90	>99	NaOH	-	-	(10)
Ni <sub>0.9</sub> Pt <sub>0.1</sub> /Ce <sub>2</sub> O <sub>3</sub>	25	43	100	-	-	28.1	(11)
Ni-0.080CeO <sub>2</sub>	50	15	99	-	2.02	51.6	(12)
Ni-Al <sub>2</sub> O <sub>3</sub> -HT	30	70	93	-	2.0	-	(13)
NiFe-alloy/MgO	26	52	99	-	-	-	(14)
NiFe/CeO <sub>2</sub>	50	28	>99	-	5.73	-	This work

Table S1 summaries the catalytic performance comparison of 2D NiFe/CeO<sub>2</sub> nanocatalyst with other reported catalysts for H<sub>2</sub> generation from N<sub>2</sub>H<sub>4</sub>•H<sub>2</sub>O decomposition. It can be clearly observed that most of the current catalysts for the decomposition of N<sub>2</sub>H<sub>4</sub>•H<sub>2</sub>O either contain noble metals or add an alkali (e.g., NaOH) to increase activity and H<sub>2</sub> selectivity, which results in a great difficulty in both equipment and operation requirements. Although some methods by employing layered double hydroxides (LDHs) to introduce solid basic sites have already been tried, such as NiFe-alloy/MgO and Ni-Al<sub>2</sub>O<sub>3</sub>-HT, the activity and selectivity remain to be further improved. In addition, 2D NiFe/CeO<sub>2</sub> multifunctional catalysts, which is composed of low cost non-noble metals NiFe as the active center and can offer an extremely large amount of Ce<sup>3+</sup> as Lewis base, have high catalytic performance and could overcome the drawbacks of aqueous alkali simultaneously.



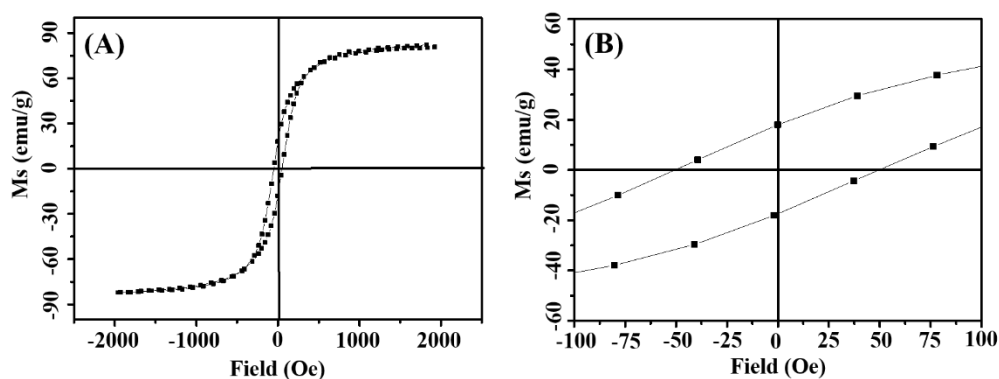
**Figure S7.** SEM image of 2D NiFe/CeO<sub>2</sub> nanocomposites after the 10th successive catalytic tests of H<sub>2</sub> generation from N<sub>2</sub>H<sub>4</sub>·H<sub>2</sub>O.

Figure S7 shows the monitored SEM images after 10 catalytic cycles of 2D NiFe/CeO<sub>2</sub> nanocomposites, which can be used to further understand the structure stability. It can be clearly seen that 2D NiFe/CeO<sub>2</sub> nanocomposites maintain the original structure basically and NiFe NPs appear slight aggregation after 10 cycles.



**Figure S8.** Recyclability tests for H<sub>2</sub> generation from N<sub>2</sub>H<sub>4</sub>·H<sub>2</sub>O catalyzed by bulk NiFe/CeO<sub>2</sub> nanocomposites.

Figure S8 illustrates the lifetime of bulk NiFe/CeO<sub>2</sub> nanocomposites, it can be clearly observed that it has a greater decrease of activity and selectivity for the H<sub>2</sub> generation from N<sub>2</sub>H<sub>4</sub>·H<sub>2</sub>O decomposition after 10 cycles than those of 2D NiFe/CeO<sub>2</sub> nanocomposites which are shown in Figure 4D, demonstrating the enhancement of the catalytic stability by the 2D-structured CeO<sub>2</sub>.



**Figure S9.** (A) Magnetic hysteresis loop of 2D NiFe/CeO<sub>2</sub> nanocomposites; (B) Magnification part hysteresis loop of 2D NiFe/CeO<sub>2</sub> nanocomposites.

As a magnetic retrievable catalyst, the hysteresis loop of the 2D NiFe/CeO<sub>2</sub> nanocomposites was plotted in Figure S9. As shown, the magnetization saturation value is 80.30 emu/g, therefore, the as-prepared 2D NiFe/CeO<sub>2</sub> nanocomposites suspended in the aqueous solution can be easily separated by an external magnet (Figure 4D inset). Moreover, it can be readily redispersed in water by stirring due to its low coercivity (53.45 Oe) and retentivity (18.05 emu/g), indicating the excellent ability of magnetic separation of 2D NiFe/CeO<sub>2</sub> nanocomposites.

## REFERENCES

- (1) Wen, M.; Wang, Y. F.; Wu, Q. S.; Jin, Y.; Cheng, M. Z. Controlled Fabrication of 0 & 2D NiCu Amorphous Nanoalloys by the Cooperation of Hard–Soft Interfacial Templates. *J. Colloid Interface Sci.* **2010**, *342*, 229–235.
- (2) Wu, D. D.; Wen, M.; Lin, X. J.; Wu, Q. S.; Gu, C.; Chen, H. X. NiCo/NiO-CoO<sub>x</sub> Ultrathin Layered Catalyst with Strong Basic Sites for High-Performance H<sub>2</sub> Generation from Hydrous Hydrazine. *J. Mater. Chem. A* **2016**, *4*, 6595-6602.
- (3) Singh, S. K.; Singh, A. K.; Aranishi, K.; Xu, Q. Noble-Metal-Free Bimetallic Nanoparticle-Catalyzed Selective Hydrogen Generation from Hydrous Hydrazine for Chemical Hydrogen Storage. *J. Am. Chem. Soc.* **2011**, *133*, 19638-19641.

- (4) Wang, H. L.; Yan, J. M.; Li, S. J.; Zhang, X. W.; Jiang, Q. Noble-Metal-Free NiFeMo Nanocatalyst for Hydrogen Generation from the Decomposition of Hydrous Hydrazine. *J. Mater. Chem. A* **2015**, *3*, 121-124.
- (5) Zhang, J. J.; Kang, Q.; Yang, Z. Q.; Dai, H. B.; Zhuang, D. W.; Wang, P. A Cost-Effective NiMoB–La(OH)<sub>3</sub> Catalyst for Hydrogen Generation from Decomposition of Alkaline Hydrous Hydrazine Solution. *J. Mater. Chem. A* **2013**, *1*, 11623-11628.
- (6) Singh, S. K.; Xu, Q. Metal–Organic Framework Supported Bimetallic Ni-Pt Nanoparticles as High-Performance Catalysts for Hydrogen Generation from Hydrazine in Aqueous Solution. *ChemCatChem* **2013**, *5*, 3000-3004.
- (7) Wang, J.; Zhang, X. B.; Wang, Z. L.; Wang, L. M.; Zhang, Y. Rhodium–Nickel Nanoparticles Grown on Graphene as Highly Efficient Catalyst for Complete Decomposition of Hydrous Hydrazine at Room Temperature for Chemical Hydrogen Storage. *Energy Environ. Sci.* **2012**, *5*, 6885-6888.
- (8) Cao, N.; Yang, L.; Du, C.; Su, J.; Luo, W.; Cheng, G. Z. Highly Efficient Dehydrogenation of Hydrazine over Graphene Supported Flower-Like Ni–Pt Nanoclusters at Room Temperature. *J. Mater. Chem. A* **2014**, *2*, 14344-14347.
- (9) Jiang, Y. Y.; Kang, Q.; Zhang, J. J.; Dai, H. B.; Wang, P. High-Performance Nickel-Platinum Nanocatalyst Supported on Mesoporous Alumina for Hydrogen Generation from Hydrous Hydrazine. *J. Power Sources* **2015**, *273*, 554-560.
- (10) Yoo, J. B.; Kim, H. S.; Kang, S. H.; Lee, B.; Hur, N. H. Hollow Nickel-Coated Silica Microspheres Containing Rhodium Nanoparticles for Highly Selective Production of Hydrogen from Hydrous Hydrazine. *J. Mater. Chem. A* **2014**, *2*, 18929-18937.
- (11) Wang, H. L.; Yan, J. M.; Wang, Z. L.; O, S.; Jiang, Q. Highly Efficient Hydrogen Generation from Hydrous Hydrazine over Amorphous Ni<sub>0.9</sub>Pt<sub>0.1</sub>/Ce<sub>2</sub>O<sub>3</sub> Nanocatalyst at Room Temperature. *J. Mater. Chem. A* **2013**, *1*, 14957-14962.
- (12) He, L.; Liang, B. L.; Li, L.; Yang, X. F.; Huang, Y. Q.; Wang, A. Q.; Wang, X. D.; Zhang, T. Cerium-Oxide-Modified Nickel as a Non-Noble Metal Catalyst for Selective Decomposition of Hydrous Hydrazine to Hydrogen. *ACS Catal.* **2015**, *5*, 1623-1628.
- (13) He, L.; Huang, Y. Q.; Wang, A. Q.; Wang, X. D.; Chen, X. W.; Delgado, J. J.; Zhang, T. A Noble-Metal-Free Catalyst Derived from Ni-Al Hydrotalcite for Hydrogen Generation from N<sub>2</sub>H<sub>4</sub>·H<sub>2</sub>O Decomposition. *Angew. Chem., Int. Ed.* **2012**, *51*, 6191-6194.
- (14) Gao, W.; Li, C. M.; Chen, H.; Wu, M.; He, S.; Wei, M.; Evans, D. G.; Duan, X. Supported Nickel–Iron Nanocomposites as a Bifunctional Catalyst towards Hydrogen Generation from N<sub>2</sub>H<sub>4</sub>·H<sub>2</sub>O. *Green Chem.* **2014**, *16*, 1560-1568.